The Astrophysical Journal Letters, 966:L28 (9pp), 2024 May 10 https://doi.org/10.3847/2041-8213/ad3336

Calcium Chemistry in Carbon-rich Circumstellar Environments: The Laboratory and Astronomical Discovery of Calcium Dicarbide, CaC_2*

H. Gupta[1,2], P. B. Changala[1], J. Cernicharo[3], J. R. Pardo[3], M. Agúndez[3], C. Cabezas[3], B. Tercero[4], M. Guélin[5], and M. C. McCarthy[1]
[1] Center for Astrophysics | Harvard & Smithsonian, Cambridge, MA 02138, USA; harshal.gupta@cfa.harvard.edu
[2] National Science Foundation, Alexandria, VA 22314, USA
[3] Instituto de Física Fundamental, CSIC, Department of Molecular Astrophysics, Serrano 121, 28006 Madrid, Spain
[4] Observatorio Astronómico Nacional, IGN, C/Alfonso XII 3, 28014 Madrid, Spain
[5] Institut de Radioastronomie Millimétrique, 300 rue de la Piscine, 38406 Saint Martin d'Hères, France
Received 2023 December 18; revised 2024 March 1; accepted 2024 March 11; published 2024 May 3

Abstract

Calcium dicarbide, CaC_2, has been characterized at high resolution in the laboratory, and its main isotopologue, $^{40}CaC_2$, has been assigned to 14 rotational emission lines between 14 and 115 GHz, including 12 previously unassigned lines, in the expanding molecular envelope of the evolved carbon star IRC+10216. Aided by high-level quantum calculations and measurements of multiple isotopologues, CaC_2 is determined to be a T-shaped molecule with a highly ionic bond linking the metal atom to the C_2 unit, very similar in structure to isovalent magnesium dicarbide (MgC_2). The excitation of CaC_2 is characterized by a very low rotational temperature of 5.8 ± 0.6 K and a kinetic temperature of 36 ± 16 K, similar to values derived for MgC_2. On the assumption that the emission originates from a 30″ shell in IRC+10216, the column density of CaC_2 is $(5.6 \pm 1.7) \times 10^{11}$ cm^{-2}. CaC_2 is only the second Ca-bearing molecule besides CaNC and only the second metal dicarbide besides MgC_2 identified in space. Owing to the similarity between the predicted ion–molecule chemistry of Ca and Mg, a comparison of the CaC_2 abundance with that of MgC_2 and related species permits empirical inferences about the radiative association–dissociative recombination processes postulated to yield metal-bearing molecules in IRC+10216 and similar objects.

Unified Astronomy Thesaurus concepts: Circumstellar envelopes (237); Carbon stars (199); Metal-containing molecules (2258); Laboratory astrophysics (2004)

1. Introduction

Metal dicarbides were long predicted to be important constituents of the atmospheres of evolved carbon stars because they are plausibly formed under thermochemical equilibrium near hot dense stellar photospheres and by nonequilibrium gas-phase processes in cool rarefied circumstellar envelopes (Tsuji 1973; Turner 1991, 1995; Petrie 1996). Characterizing their distribution, excitation, and abundance can thus shed light on poorly understood processes such as dust formation and the incorporation of metals into gas-phase molecules by ion–molecule reactions in carbon-rich circumstellar environments. Despite their perceived importance, metal dicarbides remained missing from the circumstellar molecular inventory primarily because little was known experimentally about the molecular structure and spectroscopic properties of the best candidates for astronomical detection, the most promising among which was magnesium dicarbide (MgC_2)—a highly polar molecule containing the most abundant main-group metallic element in space, Mg. We recently measured the rotational spectrum of MgC_2 at high resolution in the laboratory and assigned this molecule as the carrier of several unidentified lines in the radio spectrum of the evolved carbon star IRC+10216 (Changala et al. 2022). The identification of MgC_2 confirms long-standing predictions of metal dicarbides as important chemical constituents of evolved stars and implies that other metal dicarbides could be detectable there with accurate laboratory data in hand.

Calcium dicarbide (CaC_2) is also a promising candidate for radio astronomical detection because Ca is the next most abundant group IIA element in space after Mg, and its circumstellar ion–molecule chemistry is expected to be similar to that of Mg (Redondo et al. 1991; Petrie 2004). The very large calculated dipole moment of CaC_2 ($\mu = 11.1$ D) and the presence of two equivalent off-axis carbon nuclei result in intense transitions between rotational energy levels of an asymmetric top with missing odd-K ladders (Figure 1). In this Letter, we report the laboratory detection of CaC_2 at centimeter wavelengths and its discovery in the radio spectrum of IRC +10216. As Figure 1 shows, the astronomical data set includes the two lowest rotational transitions that were also measured to high precision in the laboratory, as well as 12 previously unassigned radio lines in the circumstellar envelope of IRC +10216, that span a wide range in energy.

The astronomical identification of CaC_2 is important in many respects. First, it adds to the scant information currently available on metal dicarbides and Ca-bearing species: CaC_2 is only the second metal dicarbide besides MgC_2 and the only Ca-bearing species after calcium isocyanide (CaNC; Cernicharo et al. 2019b)

* This work is based on observations done using the 100 m Green Bank Telescope (GBT), the Yebes 40 m telescope (projects 19A010, 20A017, 20B014, and 21A019), and the IRAM 30 m telescope. The 100 m GBT is an instrument of the Green Bank Observatory, which is a major research facility funded by the National Science Foundation and operated by Associated Universities, Inc. The Yebes 40 m radio telescope at Yebes Observatory is operated by the Spanish National Geographic Institute (Instituto Geográfico Nacional, IGN). IRAM is supported by INSU/CNRS (France), Max-Planck-Gesellschaft (MPG; Germany), and IGN (Spain).

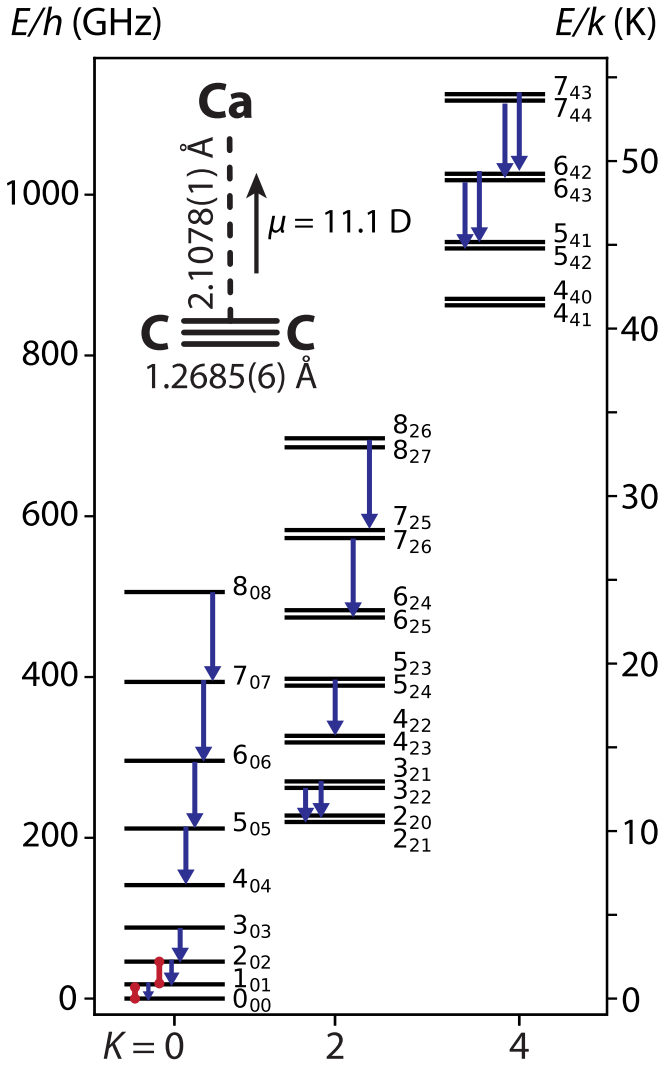

Figure 1. Lower rotational energy levels of CaC_2. Red dumbbells indicate the observed laboratory transitions, and blue arrows indicate the astronomical transitions. The inset shows the semi-experimental equilibrium structure.

detected in space. Second, Ca is the most heavily depleted element observed in IRC+10216, with an inferred depletion similar to that in interstellar clouds (Mauron & Huggins 2010), so enlarging the number of molecules that are the gas-phase reservoirs of Ca would likely advance our understanding of how some of the most refractory elements are processed in space. Finally, the observed abundance of CaC_2 relative to that of MgC_2, Mg-carbon chain radicals, and Mg-carbon chain ionic intermediates recently detected in IRC+10216 (Changala et al. 2022; Cernicharo et al. 2023) enables a more complete assessment of the most important ion–molecule pathways to metal dicarbides in circumstellar environments.

2. Laboratory Measurements

Given the intense emission features of MgC_2 in IRC+10216 and the highly accurate quantum chemical predictions (∼0.1%) possible for metal dicarbides, we initially searched for spectroscopic evidence of CaC_2 directly in the recent 6–11 mm survey of this source by Pardo et al. (2022). The only transitions expected in the survey are the $J_{K_a,K_c} = 3_{03} - 2_{02}$, $3_{22} - 2_{21}$, and $3_{21} - 2_{20}$ lines predicted at 42353, 42413, and 42474 MHz, respectively, based on our ab initio rovibrational calculations (see Appendix A). Three strong, unassigned emission features were soon after identified at 42340, 42399, and 42461 MHz, each only 0.03% lower than the predictions. The three lines display the expected intensity ratio (∼2:1:1) in the optically thin limit and a similar velocity profile to MgC_2 (Changala et al. 2022). Based on this evidence, they were tentatively assigned to CaC_2.

Evidence was then sought for the laboratory rotational lines of CaC_2 using a cavity Fourier transform microwave (FTMW) spectrometer coupled to a laser ablation–electric discharge supersonic expansion source previously used to characterize small metal-containing molecules (Brünken et al. 2008; Zingsheim et al. 2017; Lee et al. 2019). The source conditions were identical to those used in our recent studies of the closely related alkaline earth metal compounds MgC_2, MgCCH, and CaCCH (Changala et al. 2022, 2023). Rotational transitions from 5 to 26 GHz were detected with the cavity spectrometer (Grabow et al. 2005; Crabtree et al. 2016), while higher-frequency transitions were probed via double resonance. We refer the reader to these previous studies for further details.

Our ab initio calculations predict the two lowest transitions of CaC_2, $J_{K_a,K_c} = 1_{01} - 0_{00}$ and $2_{02} - 1_{01}$ to lie at 14138.7 and 28261.8 MHz. On the assumption of a fractional error of 0.03% found for the ab initio prediction of the $3_{03} - 2_{02}$ transition frequency and the tentatively assigned astronomical line (42353 MHz versus 42340 MHz), the scaled frequencies of the $1_{01} - 0_{00}$ and $2_{02} - 1_{01}$ transitions are predicted to be 14134 ± 1 MHz and 28253 ± 1 MHz. Indeed, an unassigned microwave line was subsequently detected at 14134.168(2) MHz in the laboratory and assigned to the $1_{01} - 0_{00}$ transition. The chemical composition and molecular properties of the carrier were then tested with a variety of assays. As the line requires the ablation laser, the carrier almost certainly contains Ca. The use of isotopic samples of DCCD and statistical $^{12}C/^{13}C$ HCCH further constrained the chemical composition of the carrier: it did not require H and likely had two C atoms. The transition was also unaffected by the application of a small magnetic field and was polarized easily with little microwave power, both of which are consistent with a closed-shell ground electronic state and large electric dipole moment ($\mu = 11.1$ D). Additional evidence that the carrier was CaC_2 and no other molecule was provided by the detection of the $2_{02} - 1_{01}$ transition via double resonance at 28252.714(4) MHz, as predicted.

Guided by the laboratory measurements of $^{40}Ca^{12}C_2$ and theoretical rovibrational predictions, the microwave transitions of six additional isotopic species were detected between 12 and 29 GHz. The isotopologues $^{42}Ca^{12}C_2$ (0.6%) and $^{44}Ca^{12}C_2$ (2.1%) were detected in natural abundance, while $^{40}Ca^{13}C^{12}C$, $^{40}Ca^{13}C_2$, $^{44}Ca^{13}C^{12}C$, and $^{44}Ca^{13}C_2$ were detected with a statistical $^{12}C/^{13}C$ HCCH precursor. The transition frequencies of each isotopologue are summarized in Table 1 and are uniformly within 0.5 MHz of the predicted isotopic shifts. The laboratory measurements are insufficient to determine the A, B, and C rotational constants independently for each isotopologue but provide enough information to derive a semi-experimental equilibrium structure, shown in Figure 1 (see Appendix A for details).

The production of Ca-bearing molecules in the laboratory ablation-discharge expansion source appears to be very similar to that of their Mg-bearing counterparts. We estimate that the number of CaC_2 molecules produced per pulse from the

Table 1
Laboratory Rotational Frequencies of CaC_2

Isotopologue	Transition $J'_{K_aK_c} - J''_{K_aK_c}$	Frequency (MHz)
$^{40}Ca^{12}C_2$	$1_{01} - 0_{00}$	14134.168(2)
	$2_{02} - 1_{01}$	28252.714(4)
$^{40}Ca^{13}C^{12}C$	$1_{01} - 0_{00}$	13767.768(2)
	$2_{02} - 1_{01}$	27519.699(4)
$^{40}Ca^{13}C_2$	$1_{01} - 0_{00}$	13430.617(2)
	$2_{02} - 1_{01}$	26844.997(4)
$^{42}Ca^{12}C_2$	$1_{01} - 0_{00}$	13896.715(2)
$^{44}Ca^{12}C_2$	$1_{01} - 0_{00}$	13680.331(2)
$^{44}Ca^{13}C^{12}C$	$1_{01} - 0_{00}$	13314.613(2)
$^{44}Ca^{13}C_2$	$1_{01} - 0_{00}$	12978.163(2)

Note. Estimated 2σ uncertainties are given in parentheses in units of the last digit.

calcium ablation target is comparable to that of MgC_2 (4×10^8) from a magnesium ablation target, while CaCCH and MgCCH (5×10^{10}) are within a factor of ~3 (Changala et al. 2022, 2023). For all four molecules, the addition of an 800 V electric discharge during the gas expansion increases production by a factor of 3–5 (Sun et al. 2010) relative to ablation alone, suggesting enhanced formation through electronically excited or ionized metal atoms (Bernath 1997).

3. Astronomical Observations

Following the laboratory work, additional evidence for CaC_2 in IRC+10216 was sought in both higher- and lower-frequency bands. The $1_{01} - 0_{00}$ and $2_{02} - 1_{01}$ lines—those measured in the laboratory—were observed using the 100 m Green Bank Telescope (GBT; see Appendix B for details). Figure 2 shows the two lines detected with the GBT alongside the three detected with the Yebes 40 m telescope.[6] The two low-frequency lines were detected with modest signal-to-noise ratios after several hours of observation at velocities close to the mean radial velocity of -26.5 km s^{-1} for IRC+10216, and their intensities are consistent with the fluxes expected with the higher gain of the GBT. A combined fit of the two laboratory lines and the three lines assigned in the Yebes 40 m survey of IRC+10216 enabled the rotational spectrum of CaC_2 to be predicted more precisely at frequencies above 43 GHz, and ultimately additional lines were assigned in an unpublished 3 mm survey with the IRAM 30 m telescope (see Cernicharo et al. 2019a for details). Using the three rotational constants and a single centrifugal distortion constant (Δ_{JK}) as free parameters and fixing the remaining distortion constants to theoretical values, lines in the $K = 0$ ladder could be predicted to within 0.25 MHz or about 1/40 of the line width at 112 GHz, and those in the $K = 2$ and $K = 4$ ladders could be predicted to within 1 MHz or about 1/10 of the line width at 115 GHz. Ultimately nine lines between 70 and 115 GHz (Figure 3) could be readily assigned to CaC_2, yielding a total of 14 lines in the 3–21 mm wavelength region.

There is no doubt that CaC_2 is the carrier of the astronomical lines displayed in Figures 2 and 3 and listed in Table 2. All lines possess the same width (~30 km s^{-1}) and exhibit the same U-shaped or flat-topped profiles characteristic of molecules residing in the molecular shell ($r \sim 15''$) of IRC +10216; Figure 2 shows an example with the $J = 16 - 15$ line of HC_5N overlaid on top of three lines detected with high signal-to-noise ratios using the Yebes 40 m telescope. Of the 14 lines, 11 are fully resolved and 3 are partially blended, but the profiles are of sufficiently high quality to allow reliable determination of line parameters even for the blended lines. As Table 3 shows, a combined fit of the laboratory and astronomical lines of $^{40}CaC_2$ to Watson's *A*-reduced Hamiltonian yields frequency residuals corresponding to a normalized rms of 0.92, demonstrating that they originate from the same molecule. Only six free parameters, the three rotational constants and three centrifugal distortion constants (along with two fixed to their theoretical values), are required to reproduce the rest frequencies and derive the spectroscopic constants listed in Table 3.

To determine the excitation temperatures and column density of CaC_2, we have adopted the same two-temperature model that was used for the analysis of MgC_2 emission in IRC+10216 (Changala et al. 2022). In our analysis, we have assumed by analogy with MgC_2 and CaNC that the CaC_2 emission originates from a shell 30″ in diameter (an assumption supported by the U-shaped or cusped profiles of the emission features) and corrected the integrated intensities of the lines given in Table 2 for telescope beam widths and beam efficiencies across the frequency range covered. We have also assumed that the CaC_2 lines are optically thin since no lines of the rarer isotopologues $^{43}CaC_2$, $^{44}CaC_2$, or any ^{13}C-bearing species were detected. The integrated intensities of CaC_2 emission lines in Figure 4 are simultaneously fit by a rotational temperature $T_{rot} = 5.8 \pm 0.6$ K within the *K* ladders and a kinetic temperature $T_{kin} = 36 \pm 16$ K across. Multiplying the *y*-intercept $\log(N/Z) = 10.10$ of the line through the $K = 0$ ladder by the effective partition function $Z(T_{rot}, T_{kin}) = 44.47$ computed numerically as a sum over states yields $N(CaC_2) = (5.6 \pm 1.7) \times 10^{11}$ cm^{-2}, where the total uncertainty results mainly from measurement and calibration errors, as well as uncertainties in the excitation temperatures derived from the two-temperature model.

4. Discussion

An examination of the excitation temperatures of CaC_2 allows several inferences about its distribution relative to MgC_2, CaNC, and other molecules in IRC+10216. The derived T_{rot} is statistically equivalent to the value $T_{rot} = 6 \pm 1$ K found for MgC_2 and the derived $T_{kin} = 36 \pm 16$ K is also consistent with that inferred from MgC_2 (22 ± 13 K; Changala et al. 2022). For highly polar prolate asymmetric tops such as CaC_2 and MgC_2 possessing radiatively segregated rotational ladders, the excitation temperature within the ladders (T_{rot}) is much lower than that across (T_{kin}) because the rate of collisional excitation is much lower than the rate of spontaneous radiative deexcitation (see Appendix B of Changala et al. 2022). The T_{kin} is remarkably similar to the value of ~35 K inferred for the outer shell (15″–20″) of IRC+10216 (Guélin et al. 2018) and to the value of 40 K inferred from a radiative transfer analysis of CaNC (Cernicharo et al. 2019b). Together with the cusped emission profiles, the derived kinetic temperature provides additional evidence that CaC_2 resides within the outer shell of IRC+10216 and is coextensive with CaNC; MgC_2; the neutral magnesium carbon chain radicals

[6] Appendix A of Cernicharo et al. (2023) gives the details of the Yebes 40 m observations.

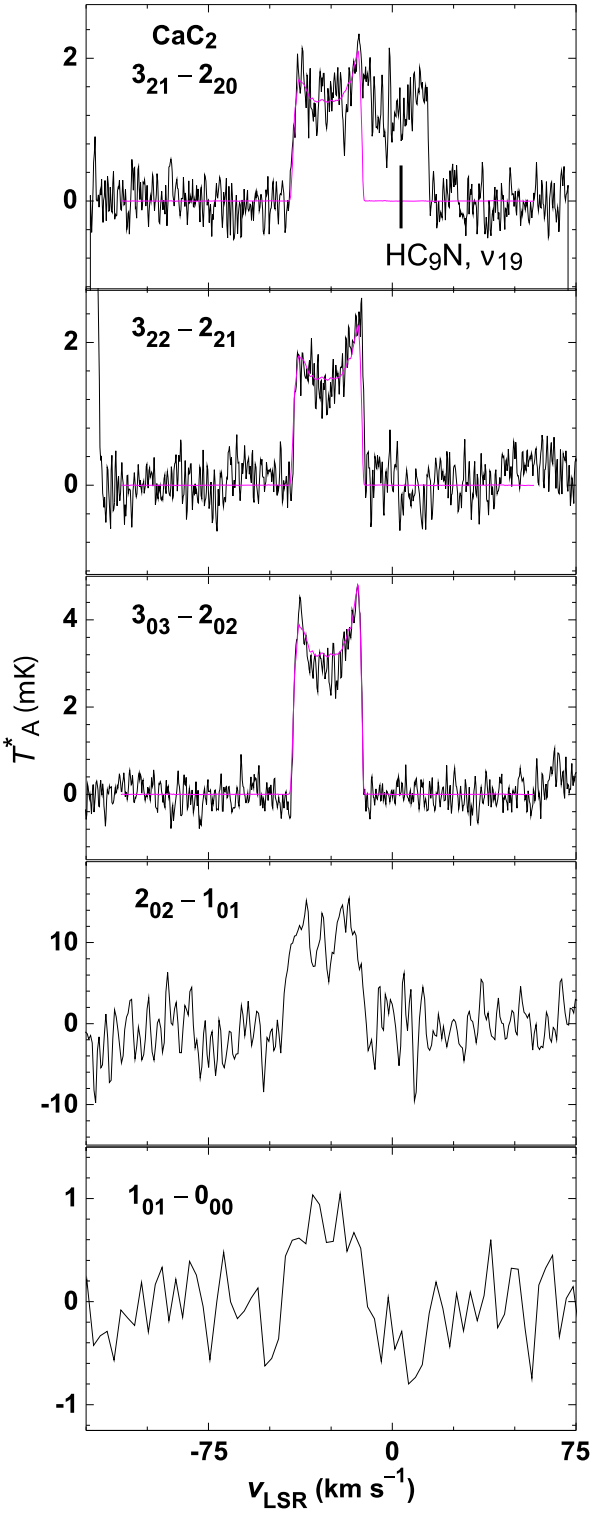

Figure 2. Rotational transitions of $^{40}CaC_2$ toward IRC+10216 in the 7–22 mm wavelength region. The bottom two spectra were observed with the 100 m GBT, and the top three were observed with the Yebes 40 m telescope. The Yebes 40 m lines are overlaid with the profile of $J = 16 - 15$ line of HC_5N (magenta trace) to show the close similarity between emission from molecules residing in the molecular shell of IRC+10216. The $1_{01} - 0_{00}$ and $2_{02} - 1_{01}$ lines were detected after 13.5 and 3.8 hr of observation; the $3_{03} - 2_{02}$, $3_{22} - 2_{21}$, and $3_{21} - 2_{20}$ lines were detected after 696 hr of observation. The $1_{01} - 0_{00}$ and $2_{02} - 1_{01}$ lines have been smoothed to 2.8 km s^{-1} and 1.4 km s^{-1}, and the $3_{03} - 2_{02}$, $3_{22} - 2_{21}$, and $3_{21} - 2_{20}$ lines have been smoothed to 1.7 km s^{-1}.

MgCCH, MgC_4H, and MgC_6H; as well as the magnesium carbon chain ions MgC_4H^+ and MgC_6H^+.

A comparison of the abundances of CaC_2, MgC_2, and other Ca- and Mg-bearing molecules allows an initial assessment of the ion–molecule pathways implicated in the formation of metal dicarbides and metal carbon chains in the outer circumstellar envelope of IRC+10216. One pathway is a two-step process consisting of radiative association (RA) of a metal ion M^+ (where M = Mg, Na, K, Al, Ca, ...) with polyynes $HC_{2n}H$ or cyanopolyynes $HC_{2n+1}N$ ($n \geqslant 3$) to form the large ionic complexes M–$HC_{2n}H^+$ and M–$HC_{2n+1}N^+$ followed by dissociative recombination (DR) of the ionic complex with electrons. This pathway was proposed by Petrie and Dunbar (Petrie 1996; Dunbar & Petrie 2002; Petrie 2004) and later used in a number of studies to reproduce the abundances of metal carbon chains in IRC+10216 (e.g., Cernicharo et al. 2019a, 2019b; Pardo et al. 2021). In our recent discovery of MgC_2, we regarded MgC_2 as a plausible DR fragmentation product of this process, concluding that the observed column density ratio MgC_2:MgCCH:MgC_4H:MgC_6H = 1:2:22:20 should help constrain the relative yields of DR of the parent ions in IRC +10216 (Changala et al. 2022), which have not yet been detected in IRC+10216. By analogy with the RA–DR mechanism involving $HC_{2n}H$, Petrie (1996) proposed that another pathway —the RA of Mg^+ with neutral carbon chain radicals $C_{2n}H$ followed by DR of Mg–$C_{2n}H^+$—should preferentially yield MgC_2 and larger carbides. The ionic intermediates in this second pathway, MgC_4H^+ and MgC_6H^+, have recently been detected in IRC+10216 (Cernicharo et al. 2023), so the observed MgC_2:MgC_4H^+:MgC_6H^+ ratio ~4:2:1 provides a direct observational constraint on the production of MgC_2. The rates of RA can be calculated reliably (Dunbar & Petrie 2002; Cernicharo et al. 2023), but a full assessment of either pathway awaits measurements of the DR-product branching ratios in the laboratory.

Since the predicted ion–molecule formation routes of Ca-bearing species are the same as those for Mg-bearing species (Petrie 2004), albeit with differences in the quantitative product branching ratios, it is possible to weigh the prospects for detection of other Ca-bearing carbon chains on the basis of the observed abundance of CaC_2. If the CaC_2:CaC_4H^+:CaC_6H^+ ratio is similar to the MgC_2:MgC_4H^+:MgC_6H^+ ratio, then the detection of the Ca-bearing ions should also be feasible because they are expected to possess comparably large dipole moments to those of MgC_4H^+ and MgC_6H^+ (Cernicharo et al. 2023). Their detection would place additional observational constraints on the production of CaC_2. Given that the column density of CaC_2 is only about a factor of 2 lower than that of MgC_2, the acetylides CaCCH, CaC_4H, and CaC_6H should also be detectable if the ratio CaC_2:CaCCH:CaC_4H:CaC_6H were similar to that of the isovalent Mg-bearing species. No calcium acetylides have yet been detected, however, and a meaningful upper limit is only available for $N(\mathrm{CaCCH}) < 1 \times 10^{11}$ cm^{-2} (Cernicharo et al. 2019b), implying CaC_2:CaCCH >28: 5, a value more than an order of magnitude higher than the MgC_2:MgCCH ratio 1: 2. By comparison, the CaC_2:CaNC ratio is about 36 times higher the MgC_2:MgNC ratio (14: 5 versus 1: 13).

It is plausible that differences between the abundance ratios of Ca- and Mg-bearing species result from the different RA–DR kinetics of Ca^+ and Mg^+ with carbon chains as can be seen from a very crude estimate of the CaNC/MgNC ratio. On

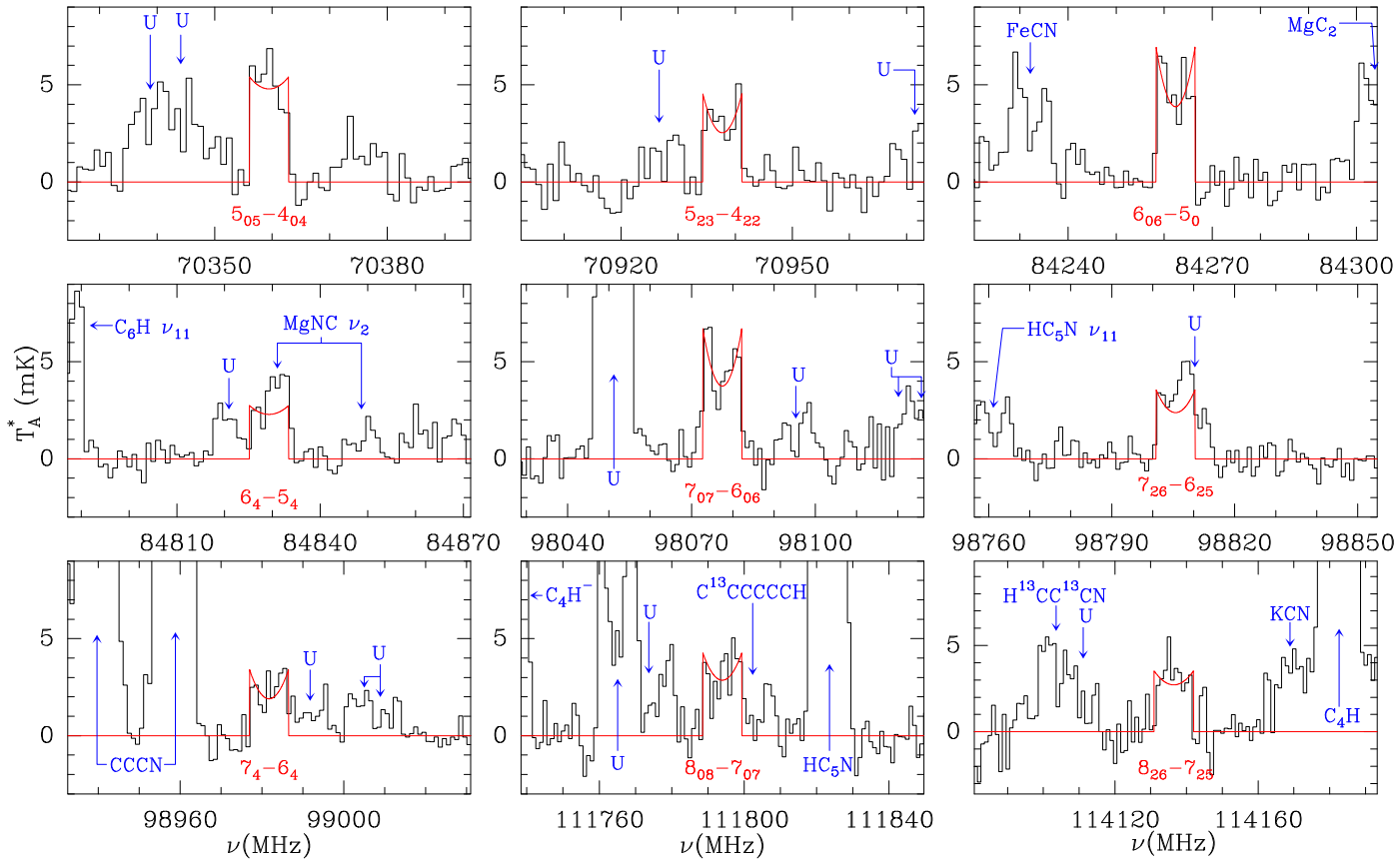

Figure 3. Rotational transitions of $^{40}CaC_2$ toward IRC+10216 in the 3 mm wavelength region observed with the IRAM 30 m telescope. Fitted profiles are plotted in red, and unidentified lines are indicated with a "U."

the assumption that the DR branching ratios of the ionic cyanopolyyne complexes with Ca and Mg are the same, Petrie (2004) estimated that the reaction of Ca^+ with cyanopolyynes to yield CaNC is only about one-fifth as efficient as the reaction of Mg^+ with cyanopolyynes to yield MgNC. The product of the reaction efficiency and the Ca^+/Mg^+ ratio, which we assume equal to the cosmic elemental abundance ratio ∼1:18 since the column densities of Mg and Mg^+ are unavailable for IRC+10216 (Mauron & Huggins 2010), yields a CaNC/MgNC ratio of ∼1:90, which is within 40% of the observed value of ≃1:65 (Cernicharo et al. 2019a). Similar studies of the thermochemistry of Ca^+ with polyynes and carbon chain radicals might help explain the abundance ratios of CaC_2 and neutral Ca-carbon chains, but the largest source of uncertainty is probably the unknown branching fractions of the DR step.

Dunbar & Petrie (2002) argued that RA–DR reactions are the dominant loss process for metal ions in IRC+10216 and speculated that they might have a significant impact on carbon chain abundances. An important consequence of RA–DR chemistry is the conversion of larger carbon chains into smaller ones. Because the rates for RA increase dramatically with molecular size and density of states, eventually approaching the collisional rate, the formation of the M^+–chain ionic complex becomes more efficient for longer chains (Dunbar & Petrie 2002; Cernicharo et al. 2023). If correct, the abundance ratio (M^+–chain)/(chain) should increase with chain length, and that is indeed what is found for the metal–carbon chain cations in IRC+10216 so far: the MgC_6H^+/C_6H ratio (0.91%) is nearly 3.5 times the MgC_4H^+/C_4H ratio (0.26%) and the MgC_5N^+/C_5N ratio (1.8%) nearly 36 times the MgC_3N^+/C_3N ratio (0.05%).[7] A higher fraction of the longer chains is thus incorporated into the corresponding ionic complexes and available for DR, resulting in a more efficient breakdown of longer chains relative to shorter ones. Quantifying the effect on carbon chain abundances requires determining the overall efficiency of the RA–DR process, which is only possible once the abundances of the major DR products including metal dicarbides are known.

There is considerable circumstantial evidence that the RA–DR mechanism is operative in the outer circumstellar envelope of IRC+10216. Mauron & Huggins (2010) measured absorption spectra of a number of elements (Na, K, Ca, Cr, and Fe) along a sight line ∼35″ from the center of IRC+10216; the ionization degree constrained by their measurements of neutral and singly ionized calcium (Ca I and Ca II) implies that substantial column densities of singly charged ions of these elements are available to undergo RA with large carbon chains. Although measurements of Mg are unavailable, Mg is expected to be ionized, and indeed the presence of four Mg-carbon chain cations—MgC_4H^+, MgC_3N^+, MgC_6H^+, and MgC_5N^+—formed via RA has recently been established in the molecular shell of IRC+10216 ($10'' \lesssim r \lesssim 20''$; Cernicharo et al. 2023); detection of Mg II would establish the degree to which it is incorporated into these species. Given the large column density of Ca II ($N(\mathrm{Ca\ II}) = 7 \times 10^{12}$ cm^{-2}; Mauron & Huggins (2010), Ca-bearing analogs of the Mg-carbon chain cations are promising candidates for detection. Similarly, if the column density of Na II is as large as

[7] Column densities are from the following references: C_4H and C_6H (Pardo et al. 2022); C_3N and C_5N (Cernicharo et al. 2000).

Table 2
Lines of CaC_2 in IRC+10216

Transition $J'_{K_aK_c} - J''_{K_aK_c}$	ν_{obs}[a] (MHz)	$\nu_{obs-calc}$ (MHz)	E_u/k (K)	S	$\int T_A^* dv$[b] (mK km s^{-1})	θ_B (arcsec)	η_B	W[c] (mK km s^{-1})
$1_{01} - 0_{00}$	14134.168[d]	0.001	0.68	1.00	22 ± 4	54.0	0.959	95 ± 19
$2_{02} - 1_{01}$	28252.714[d]	0.000	2.03	2.00	334 ± 23	26.8	0.918	654 ± 80
$3_{03} - 2_{02}$	42340.05 ± 0.04	−0.016	4.07	3.00	92 ± 9	42.5	0.53	520 ± 52
$3_{22} - 2_{21}$	42399.12 ± 0.04	0.035	12.77	1.67	46 ± 5	42.5	0.53	259 ± 27
$3_{21} - 2_{20}$	42460.92 ± 0.04	−0.073	12.77	1.67	45 ± 5	42.5	0.53	258 ± 26
$5_{05} - 4_{04}$	70359.45 ± 0.20	−0.195	10.15	4.98	145 ± 17	35.0	0.853	400 ± 47
$5_{23} - 4_{22}$	70937.86 ± 0.20	−0.200	18.89	4.20	96 ± 14	34.7	0.853	255 ± 37
$6_{06} - 5_{05}$	84262.30 ± 0.20	−0.394	14.19	6.00	142 ± 16	29.2	0.853	324 ± 36
$6_{43} - 5_{42}$[d]	84829.20 ± 0.20	−0.017	49.03	3.33	35 ± 8	29.0	0.853	80 ± 18
$6_{42} - 5_{41}$[d]	84829.20 ± 0.20	−0.063	49.03	3.33	35 ± 8	29.0	0.853	80 ± 18
$7_{07} - 6_{06}$	98077.46 ± 0.20	0.113	18.90	6.99	137 ± 16	25.1	0.853	273 ± 31
$7_{26} - 6_{25}$	98805.58 ± 0.30	−0.103	27.68	6.43	76 ± 9	24.9	0.853	150 ± 19
$7_{44} - 6_{43}$[e]	98981.70 ± 0.20	0.239	53.78	4.71	35 ± 7	24.9	0.853	69 ± 13
$7_{43} - 6_{42}$[e]	98981.70 ± 0.20	0.085	53.78	4.71	35 ± 7	24.9	0.853	69 ± 13
$8_{08} - 7_{07}$	111793.80 ± 0.20	0.107	24.27	7.99	96 ± 12	22.0	0.853	174 ± 23
$8_{26} - 7_{25}$	114136.85 ± 0.20	0.080	33.25	7.50	38 ± 9	21.6	0.853	68 ± 16

Notes. Unless otherwise noted, estimated uncertainties are 1σ. Frequencies subtracted from those observed are calculated from the constants in Table 3. E_u is the energy of the upper state of the transition, and S is the asymmetric rotor line strength. $\alpha_{J2000} = 09^h47^m57^s.36$, $\delta_{J2000} = +13°16'44''.4$.
[a] On the assumption of $v_{LSR} = -26.5$ km s^{-1}.
[b] Derived from least-squares fits of shell profiles to the spectra shown in Figures 3; in some cases the expansion velocity was fixed to 14.5 km s^{-1}.
[c] $W = \int T_A^* dv / \eta_B f_D$, where $f_D = \theta_S^2/(\theta_S^2 + \theta_B^2)$ and the source diameter $\theta_S = 30''$. Errors include calibration uncertainties of 10% and an assumed error of 1 D on the dipole moment, added in quadrature.
[d] Rest frequency from Table 1 used to calculate the radial velocity of the line.
[e] Unresolved doublet with each component assumed to lie at the same frequency and possess half the intensity.

Table 3
Molecular Constants of $^{40}CaC_2$

Constant	Value
A...	52371(1)
$(B + C)/2$...	7067.09327(89)
$(B - C)/4$...	242.109(37)
$10^3\Delta_J$...	4.771(72)
$10^3\Delta_{JK}$...	127.05(79)
$10^3\Delta_K$...	73.772[a]
$10^3\delta_J$...	0.66(41)
$10^3\delta_K$...	71.831[a]
σ_{nrms}...	0.92
Δ...	0.1958(8)

Note. Constants are derived from a least-squares fit to the rotational transitions in Tables 1 and 2. Rotational and centrifugal distortion constants are given in units of MHz, the normalized rms (σ_{nrms}) is dimensionless, and the inertial defect (Δ) is in amu-Å^2. The 1σ uncertainties are indicated in parentheses in units of the last decimal place. Parameters for which no uncertainties are indicated have been fixed to the theoretical values.
[a] Second-order vibrational perturbation theory value at the CCSD(T)/cc-pCVQZ level of theory.

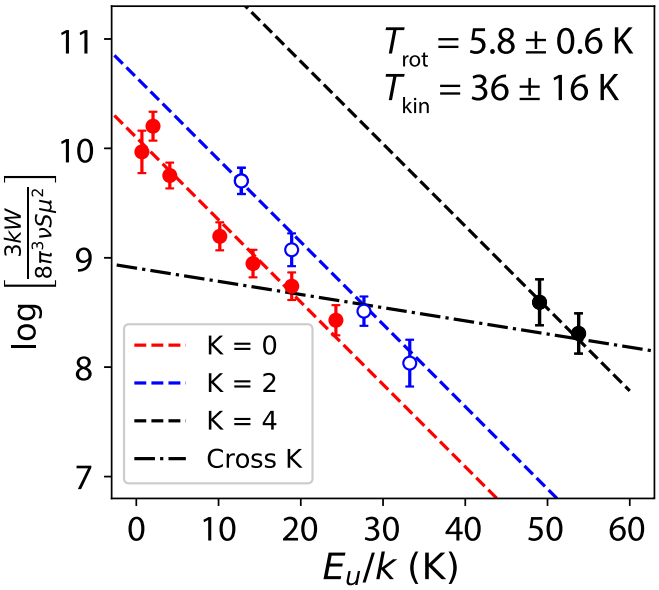

Figure 4. Rotational temperature diagram of $^{40}CaC_2$ in IRC+10216, fitted with the two-temperature model described in Changala et al. (2022). The slope of the parallel lines through each K ladder gives the rotational temperature (T_{rot}), and that of the line through points across the K ladders gives the kinetic temperature (T_{kin}). The flux of the $K = 4$ transitions is assumed to be one-half the total flux of the unresolved doublets listed in Table 2. The error bar on each data point is twice the error shown in Table 2. Error bars on the parameters are twice the standard error of the fit.

that inferred by Mauron & Huggins (2010; $N(\text{Na II}) = 10^{14}$ cm^{-2}), then it is plausible that Na-bearing cations are also detectable and might help explain the presence of molecules such as NaCCCN, which has recently been detected (Cabezas et al. 2023). While the RA–DR mechanism might account for many metal-bearing molecules in the outer envelope of IRC +10216, other formation mechanisms may also need to be considered for species such as the cyanides NaCN, KCN, AlNC, and FeCN, and the carbide FeC whose distributions are inferred to peak within or extend into warmer, denser regions closer to the central star in IRC+10216 ($5'' \lesssim r \lesssim 10''$; Pulliam et al. 2010 and references therein; Zack et al. 2011; Koelemay & Ziurys 2023 and references therein).

The laboratory detection of CaC_2 adds a critical new data point for understanding the structure and bonding of metal

dicarbides, which has important implications on both fundamental chemistry and on identifying other metal-bearing species that are likely candidates for radio astronomical detection and best constrain the chemistry of circumstellar environments. Like isovalent MgC_2, CaC_2 is T-shaped and exhibits a highly ionic metal–carbon bond best described as $Ca^{2+}-C_2^{2-}$. This effective oxidation state is reflected in the large dipole moments of alkaline earth dicarbides (MgC_2 ∼7.9 D; Itono et al. (2000); CaC_2 ∼11.1 D), which are similar to other metal-ligand compounds of dominant $M^{2+}L^{2-}$ character (e.g., MgO ∼6.2 D, Büsener et al. 1987; CaO ∼9.5 D, Khalil et al. 2011) and much larger than singly ionic M^+L^- compounds (e.g., MgCCH ∼1.8 D, Changala et al. 2023; CaCCH ∼3.0 D, Marr et al. 1995). The equilibrium CC bond length, $r_{CC} = 1.2685(6)$ Å, is only marginally shorter than the CC bond length in MgC_2, $r_{CC} = 1.2706(7)$ Å, both of which are nearly identical to the bond length of the free C_2^- monoanion, $r_{CC} = 1.26831(13)$ Å (Rehfuss et al. 1988; the free dianion is electronically unstable, Gulania et al. 2019). The CC bond length in neutral C_2, $r_{CC} = 1.24244(1)$ Å (Douay et al. 1988) is significantly shorter than that in free C_2^-, $Mg^{2+}C_2^{2-}$, and $Ca^{2+}C_2^{2-}$. The ground electronic state of C_2 is dominated by two main orbital configurations, $\Psi \sim 0.8 \times |(1\pi_u)^4(2\sigma_u)^2| - 0.3 \times |(1\pi_u)^4(3\sigma_g)^2|$ (Shaik et al. 2012; Jiang et al. 2022). The latter term introduces a partial vacancy in the strongly antibonding $2\sigma_u$ orbital, which contributes to a contraction of the C_2 bond length relative to what might be expected from the dominant configuration alone. In $Ca^{2+}C_2^{2-}$, this vacancy in the C_2 ligand is filled, which thereby increases the CC bond length. Electrostatic repulsion of the excess negative charge contributes to further CC bond lengthening. These features of ionic metal–carbon bonding will influence the structure and spectroscopic signatures of larger magnesium and calcium carbides that are plausible fragmentation products of RA–DR processes, such as cyclic and linear isomers of MC_3, MC_4, and higher analogs (Redondo et al. 2003a, 2003b; Agbaglo et al. 2022). The basic structural patterns established here for the comparatively simple MC_2 molecules will provide a useful point of reference for quantum chemical predictions of the spectroscopic parameters needed for their astronomical detection.

Experimental and theoretical studies of the most important species in the ion–molecule pathways operative in circumstellar environments are needed to guide astronomical searches, which will in turn advance our understanding of the production of metal-bearing molecules in space. A natural extension of the present work is the characterization of larger carbides of Mg and Ca. It has been suggested that metal carbides containing an even number of carbon atoms are among the main products in the DR of $MgC_{2n}H^+$, viz., MgC_4 and MgC_6 (Petrie 1996), and by analogy, CaC_4 and CaC_6 are plausible products of the DR of $CaC_{2n}H^+$. Theoretical studies indicate that the even-carbon clusters tend to be cyclic and possess closed-shell electronic ground states (Redondo et al. 2003a, 2003b; Agbaglo et al. 2022), which might favor their astronomical detection. Quantum calculations employing high levels of theory are imperative to accurately predict their structures and guide searches. There is precedent for the detection of a large silicon-bearing carbide SiC_4 in IRC+10216, for which similar ion–molecule pathways have been proposed (Ohishi et al. 1989), and it is highly desirable that the ionic intermediates and products of the postulated pathways be characterized. There are additional ion–molecule pathways, such as the mutual neutralization of metal ions and carbon chain anions, which remain to be investigated, and which might yield products and branching ratios that are distinct from the DR of ion–molecule complexes. Since MgC_4H^+, MgC_6H^+, MgC_3N^+, and MgC_5N^+ have already been detected in IRC+10216, it is likely that their Ca-bearing analogs, as well as larger metal–carbon chains containing C_8H and C_7N, also await detection there with more sensitive observations (Cernicharo et al. 2023). Molecular ions and metal-bearing species are difficult to produce in laboratory sources, however, so the laboratory detection of metal-bearing molecular ions might pose an even greater challenge and require more efficient production methods. In recent years, quantum calculations have led the way in the identification of new linear metal-bearing species including ions in IRC+10216 (Cernicharo et al. 2023), so accurate theoretical characterization will continue to be important in guiding astronomical searches.

Within the context of recent astronomical discoveries, the discovery of CaC_2 suggests a number of important avenues for investigation. High priority should be given to the search for $CaC_{2n}H^+$ cations, as their detection will establish a direct observational link between the cations formed via RA and metal carbides such as CaC_2, especially since the Ca II abundance is available from optical observations (Mauron & Huggins 2010). The fate of molecules such as CaC_2 outside the molecular shell of IRC+10216 is poorly understood. Characterizing the radial distribution, excitation, and abundance of CaC_2 within IRC+10216 at high angular resolution might shed light on physicochemical processes occurring close to the central star if some CaC_2 forms and remains in the gas phase in regions hotter than its condensation temperature of ∼1600 K (Gilman 1969); such studies might complement studies of other refractory species such as FeC that are thought to form and reside in the inner regions of the circumstellar envelope (Koelemay & Ziurys 2023). Sensitive observations sampling the extended outer envelope ($r > 20''$) and targeting related carbides such as CaC and MgC might yield their detection, permitting comparisons with similar systems such as SiC, which is thought to be a photodissociation product of SiC_2 and thus exhibits a more extended distribution (Apponi et al. 1999). Such studies might elucidate the processing of circumstellar material before it is expelled into the interstellar medium. A deep search for CaC_2 and MgC_2 within chemically rich interstellar clouds might not be premature given that SiC_2 has recently been detected in a molecular cloud where shocks are thought to release refractory elements into the gas phase (Massalkhi et al. 2023); since both CaC_2 and MgC_2 possess very large dipole moments, such searches could be undertaken in absorption against bright radio continuum sources.

Acknowledgments

We thank Dr. Carl Gottlieb (CfA) for helpful discussions and Dr. David Frayer (GBO) for advice on the GBT data reduction. P.B.C. and M.C.M. are supported by the National Science Foundation (award Nos. AST-1908576 and PHY-2110489). We acknowledge funding support from the Spanish Ministerio de Ciencia e Innovación through grants PID2019-107115GB-C21, PID2019-106110GB-100, and PID2022-137980NB-I00. We also thank the European Research Council for funding

through grant ERC-2013-Syg610256-NANOCOSMOS. H.G. acknowledges support from the National Science Foundation for participation in this work as part of his independent research and development plan. Any opinions, findings, and conclusions expressed in this material are those of the authors and do not necessarily reflect the views of the National Science Foundation.

Appendix A
Structure Calculations and Semi-experimental Equilibrium Geometry

Coupled cluster calculations were performed using the CFOUR package (Matthews et al. 2020; Stanton et al. 2020) at the singles, doubles, and perturbative triples (CCSD(T)) level of theory (Raghavachari et al. 1989) with correlation-consistent core-valence basis sets, cc-pCV*X*Z ($X = $ D, T, Q, 5) basis sets (Koput & Peterson 2002), correlating all but the Ca 1*s*, 2*s*, and 2*p* inner-core electrons. The complete basis set (CBS) limit of the equilibrium geometry was estimated by an exponential extrapolation of the $X = $ T–5 sequence. To derive a semi-experimental equilibrium geometry, vibrational corrections to the rotational frequencies were determined by variational rovibrational calculations on a potential energy surface fitted to ca. 450 CCSD(T)/cc-pCVQZ single-point energies using the NITROGEN package (Changala 2021). The electronic *g*-tensor corrections to the rotational constants (Gauss & Puzzarini 2010) were also computed at the same level of theory. The CCSD(T)/cc-pCV5Z equilibrium dipole moment is 11.1 D.

As with MgC_2 (Changala et al. 2022), the small number of laboratory transitions observed for each isotopologue was insufficient to determine a complete set of experimental rotational constants. The structure determination was instead performed by least-squares fitting directly to the transition frequencies accounting for the variationally computed vibrational corrections (which include centrifugal distortion effects) and the rotational *g*-tensor. The optimized structural parameters are shown in Figure 1 and are compared to the extrapolated CCSD(T) geometry in Table 4. These parameters reproduce the 10 laboratory frequencies with an rms residual of 40 kHz.

Table 4
The Equilibrium Geometry of CaC_2

Basis Set	r_{CC} (Å)	r_{CaC_2} (Å)
D	1.29269	2.15761
T	1.27305	2.12711
Q	1.26931	2.11432
5	1.26839	2.10988
CBS	1.26810	2.10751
r_{se}	1.2685(6)	2.1078(1)

Note. The CCSD(T)/cc-pCV*X*Z bond lengths (in Å) are shown for $X = $ D–5, followed by the complete basis set (CBS) limit estimated from an exponential extrapolation of $X = $ T–5. The semi-experimental equilibrium geometry (r_{se}) was determined as discussed in the text. r_{CC} is the C-C distance, and r_{Ca-C_2} is the distance between Ca and the CC center of mass.

Appendix B
Observations with the 100 m GBT

Observations of the $1_{01} - 0_{00}$ and $2_{02} - 1_{01}$ rotational transitions of CaC_2 were undertaken with the *Ku* band (12–15.4 GHz) and *Ka* band MM-F1 (26–31 GHz) receivers of the GBT between 2022 November and 2023 July as part of projects GBT22B-287 and GBT23A-432. The VErsatile GBT Astronomical Spectrometer was configured for simultaneous observations of four frequency windows, each 850 MHz wide, at a frequency resolution of 66 kHz. Both polarizations were observed at *Ku* band, while only one polarization was observed at *Ka* band. System temperatures were typically 25–32 K at *Ku* band and 65–72 K at *Ka* band. Spectra at *Ku* band were taken by nodding for 90 s with a beam throw of 330″ in azimuth and at *Ka* band by position switching for 90 s with the OFF position lying 330″ in azimuth relative to IRC+10216 ($\alpha_{J2000} = 09^h47^m57\overset{s}{.}36$, $\delta_{J2000} = +13°16'44\overset{''}{.}4$). The beam widths (FWHM) are about 54″ at 14.1 GHz and 27″ at 28.2 GHz (Table 2). The pointing and focusing of the telescope were checked about every 90 minutes by observing a strong nearby continuum source (0750+1231 or 0854+2006); the pointing was found to be generally good to 5″. Intensities at all frequencies were calibrated by observing the quasar 3C 286.

ORCID iDs

H. Gupta https://orcid.org/0000-0003-2588-516X
P. B. Changala https://orcid.org/0000-0003-0304-9814
J. Cernicharo https://orcid.org/0000-0002-3518-2524
J. R. Pardo https://orcid.org/0000-0003-4639-8440
M. Agúndez https://orcid.org/0000-0003-3248-3564
C. Cabezas https://orcid.org/0000-0002-1254-7738
B. Tercero https://orcid.org/0000-0002-4782-5259
M. C. McCarthy https://orcid.org/0000-0001-9142-0008

References

Agbaglo, D. A., Cheng, Q., Fortenberry, R. C., Stanton, J. F., & DeYonker, N. J. 2022, JPCA, 126, 4132
Apponi, A. J., McCarthy, M. C., Gottlieb, C., & Thaddeus, P. 1999, ApJ, 516, L103
Bernath, P. F. 1997, Advances in Photochemistry, 23, 1
Brünken, S., Müller, H. S. P., Menten, K. M., McCarthy, M. C., & Thaddeus, P. 2008, ApJ, 676, 1367
Büsener, H., Heinrich, F., & Hese, A. 1987, CP, 112, 139
Cabezas, C., Pardo, J. R., Agúndez, M., et al. 2023, A&A, 672, L12
Cernicharo, J., Cabezas, C., Pardo, J., et al. 2019a, A&A, 630, L2
Cernicharo, J., Velilla-Prieto, L., Agúndez, M., et al. 2019b, A&A, 630, L4
Cernicharo, J., Cabezas, C., Pardo, J. R., et al. 2023, A&A, 672, L13
Cernicharo, J., Guélin, M., & Kahane, C. 2000, A&AS, 142, 181
Changala, P. B. 2021, NITROGEN, version 2.1.2, Zenodo, doi:10.5281/zenodo.7342277
Changala, P. B., Genossar-Dan, N., Brudner, E., et al. 2023, PNAS, 120, e2303586120
Changala, P. B., Gupta, H., Cernicharo, J., et al. 2022, ApJL, 940, L42
Crabtree, K. N., Martin-Drumel, M.-A., Brown, G. G., et al. 2016, JChPh, 144, 124201
Douay, M., Nietmann, R., & Bernath, P. F. 1988, JMoSp, 131, 250
Dunbar, R. C., & Petrie, S. 2002, ApJ, 564, 792
Gauss, J., & Puzzarini, C. 2010, MolPh, 108, 269
Gilman, R. C. 1969, ApJL, 155, L185
Grabow, J. U., Palmer, E. S., McCarthy, M. C., & Thaddeus, P. 2005, RScI, 76, 093106
Guélin, M., Patel, N. A., Bremer, M., et al. 2018, A&A, 610, A4
Gulania, S., Jagau, T.-C., & Krylov, A. I. 2019, FaDi, 217, 514
Itono, S., Takano, K., Hirano, T., & Nagashima, U. 2000, ApJL, 538, L163
Jiang, J., Ye, H. Z., Nauta, K., et al. 2022, JPCA, 126, 3090
Khalil, H., Brites, V., Quéré, F. L., & Léonard, C. 2011, CP, 386, 50

Koelemay, L. A., & Ziurys, L. M. 2023, ApJL, 958, L6
Koput, J., & Peterson, K. A. 2002, JPCA, 106, 9595
Lee, K. L. K., Thorwirth, S., Martin-Drumel, M. A., & McCarthy, M. C. 2019, PCCP, 21, 18911
Marr, A. J., Perry, J., & Steimle, T. C. 1995, JChPh, 103, 3861
Massalkhi, S., Jiménez-Serra, I., Martín-Pintado, J., et al. 2023, A&A, 678, A45
Matthews, D. A., Cheng, L., Harding, M. E., et al. 2020, JChPh, 152, 214108
Mauron, N., & Huggins, P. J. 2010, A&A, 513, A31
Ohishi, M., Kaifu, N., Kawaguchi, K., et al. 1989, ApJL, 345, L83
Pardo, J. R., Cabezas, C., Fonfría, J. P., et al. 2021, A&A, 652, L13
Pardo, J. R., Cernicharo, J., Tercero, B., et al. 2022, A&A, 658, A39
Petrie, S. 1996, MNRAS, 282, 807
Petrie, S. 2004, AJCh, 57, 67
Pulliam, R. L., Savage, C., Agúndez, M., et al. 2010, ApJL, 725, L181
Raghavachari, K., Trucks, G. W., Pople, J. A., & Head-Gordon, M. 1989, CPL, 157, 479
Redondo, P., Barrientos, C., Cimas, A., & Largo, A. 2003a, JPCA, 107, 4676
Redondo, P., Barrientos, C., Cimas, A., & Largo, A. 2003b, JPCA, 107, 6317
Redondo, R., Ellinger, Y., Berthier, G., & Cimiraglia, R. 1991, A&A, 247, L1
Rehfuss, B. D., Liu, D. J., Dinelli, B. M., et al. 1988, JChPh, 89, 129
Shaik, S., Danovich, D., Wu, W., et al. 2012, NatCh, 4, 195
Stanton, J. F., Gauss, J., Cheng, L., et al. 2020, CFOUR, Coupled-Cluster Techniques for Computational Chemistry, a quantum-chemical Program Package, http://cfour.de
Sun, M., Halfen, D. T., Min, J., et al. 2010, JChPh, 133, 174301
Tsuji, T. 1973, A&A, 23, 411
Turner, B. E. 1991, ApJ, 376, 573
Turner, B. E. 1995, Ap&SS, 224, 297
Zack, L. N., Halfen, D. T., & Ziurys, L. M. 2011, ApJL, 733, L36
Zingsheim, O., Martin-Drumel, M. A., Thorwirth, S., et al. 2017, J. Phys. Chem. Lett., 8, 3776